


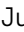




Cite this: *J. Mater. Chem. A*, 2024, 12, 20215

# Electrochemical performance of $M(\text{dca})_2\text{pyz}$ ( $M = \text{Fe}, \text{Co}$ and $\text{Ni}$ ) MOFs as sustainable anodes in lithium-ion batteries†

Isabel Ciria-Ramos, <sup>ab</sup> Alberto García-Fernández, <sup>c</sup> Álvaro Mayoral, <sup>a</sup> Alodia Orera, <sup>a</sup> Emilio J. Juárez-Perez <sup>\*ad</sup> and Marta Haro <sup>\*ab</sup>

A family of Metal–Organic Frameworks (MOFs) based on the ligands pyrazine (pyz) and dicyanamide (dca) and the metal centers Fe, Co and Ni with the unit formula  $M(\text{dca})_2\text{pyz}$  has been studied as anodes for Li-Ion Batteries (LIBs). These compounds are analogs of transition metal nitrides (TMNs) but synthesized following an environmentally friendly process.  $\text{Fe}(\text{dca})_2\text{pyz}$  provides the best electrochemical performance with a specific capacity of  $519 \text{ mA h g}^{-1}$  and  $375 \text{ mA h cm}^{-3}$  after 450 cycles at  $200 \text{ mA g}^{-1}$  and a capacity retention of 90% with respect to the first cycle. This performance is better than most of the Fe nitrides reported to date, highlighting its potential as an anode for LIBs. The high capacity is due to the conversion and displacement reaction occurring with the Fe atoms and the insertion of  $\text{Li}^+$  into the ligands. In contrast, the specific capacities of  $\text{Co}(\text{dca})_2\text{pyz}$  and  $\text{Ni}(\text{dca})_2\text{pyz}$  are lower due to a partial reduction of the Co atoms in the first case, and to the oxidation of the Ni atoms which hinders the  $\text{Li}^+$  intercalation process in the second. As a result, the specific capacities after 450 cycles at  $200 \text{ mA g}^{-1}$  are  $148 \text{ mA h g}^{-1}$  for  $\text{Co}(\text{dca})_2\text{pyz}$  and  $57 \text{ mA h g}^{-1}$  for  $\text{Ni}(\text{dca})_2\text{pyz}$ . Powder-XRD and TEM characterizations after cycling of the three samples reveal that  $\text{Fe}(\text{dca})_2\text{pyz}$  and  $\text{Co}(\text{dca})_2\text{pyz}$  samples become amorphous while the  $\text{Ni}(\text{dca})_2\text{pyz}$  material does not. This suggests that the amorphization process is relevant for obtaining anodes with improved electrochemical performance. This study demonstrates that MOFs obtained by a cost-effective and environmentally friendly method can act as precursors for obtaining high performance anodes for LIBs without the need for an energy intensive carbonization process, since they undergo an *in situ* amorphization process, giving rise to AMorphous Organometallic (AMO) electrodes.

Received 31st March 2024  
Accepted 2nd July 2024

DOI: 10.1039/d4ta02137a

rsc.li/materials-a

## 1 Introduction

The growing environmental problems associated with the use of fossil fuels urgently require a transition from traditional energy sources to clean, safe and renewable energy sources. Among the diverse technologies available for this objective, LIBs stand out as a promising alternative. Their capacity to store significant amounts of both volumetric and gravimetric energy density, resulting from the high reduction potential and compact size of  $\text{Li}^+$ , positions them as a noteworthy solution. Commercial LIBs commonly employ graphite as an anode due to its notable

theoretical specific capacity of  $370 \text{ mA h g}^{-1}$ , low operating potential ( $\sim 0.1 \text{ V vs. Li/Li}^+$ ), and relatively modest cost (8–13 USD per kg).<sup>1</sup> However, the production of battery-grade graphite involves resource and energy-intensive processes, including mining and purifying natural graphite or converting high-quality petroleum distillate bottoms into synthetic graphite.<sup>2,3</sup> Additionally, the graphite anode is recognized as a significant impediment to the fast-charging capability of commercially available LIBs.<sup>4</sup> This is attributed to the sluggish lithium-ion intercalation kinetics of the graphite bulk phase and its lower redox potential, leading to favorable lithium deposition during fast-charging or at low temperatures. This not only degrades electrochemical performance but also raises safety concerns. Thus, despite the clear suitability of graphite as an anode for LIBs in portable electronic devices, it cannot fulfill the requirements of high-performance batteries.

As an alternative to graphite, transition metal nitrides (TMNs) present promising characteristics for anode applications, such as high theoretical capacities, natural abundance, low cost, and good lithium diffusion that promotes pseudocapacitive behavior.<sup>5–8</sup> Furthermore, TMNs present chemical stability, relatively high conductivity, simple synthesis

<sup>a</sup>Instituto de Nanociencia y Materiales de Aragón (INMA), CSIC-Universidad de Zaragoza, Zaragoza, 50009, Spain. E-mail: mharo@unizar.es; ejuarezperez@unizar.es

<sup>b</sup>Departamento de Química Física, Facultad de Ciencias, Universidad de Zaragoza, Plaza San Francisco, Zaragoza, 50009, Spain

<sup>c</sup>Division of Applied Physical Chemistry, Department of Chemistry, KTH Royal Institute of Technology, SE-100 44 Stockholm, Sweden

<sup>d</sup>Aragonesse Foundation for Research and Development (ARAID). Government of Aragón, Zaragoza, 50018, Spain

† Electronic supplementary information (ESI) available. See DOI: <https://doi.org/10.1039/d4ta02137a>

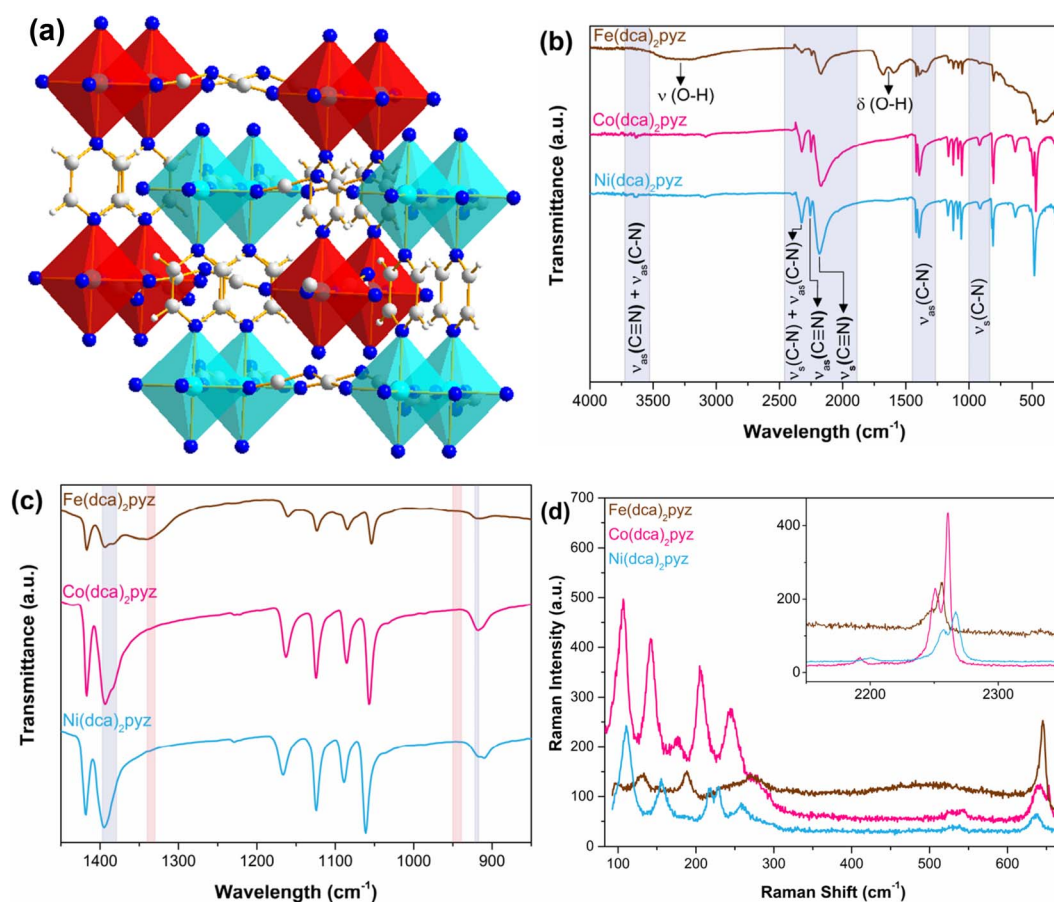


processes and their conversion reaction occurs at low potentials.<sup>7,9–12</sup> Nevertheless, these materials have the main limitation attributed to conversion electrodes, which is the drastic volume changes during cycling that give rise to a poor cyclability.<sup>5,6,8–10,12,13</sup> To solve this problem several strategies have been followed such as reducing the size of TMNs to obtain nanoparticles,<sup>10,14</sup> designing composites with different carbon containing materials,<sup>5,6,8,10,12,15</sup> depositing the active materials in conductive substrates,<sup>12,13,16</sup> using graphene oxide as a scaffold that contains the TMNs<sup>7,9,11,17</sup> or fabricating porous structures.<sup>14,18</sup> Even though these strategies can obtain pretty good results, they usually require heating the samples at high temperatures or using environmentally aggressive reducing agents for reducing graphene oxide. This not only has an environmental impact, but also a cost effect in regard to a future commercialization of the electrodes.

An alternative approach involves the utilization of Metal–Organic Frameworks (MOFs) as environmentally friendly and electrochemically competitive electrodes for LIBs. MOFs, composed of metallic centers connected to organic ligands, have garnered growing attention as LIB electrodes. This heightened interest stems from their facile pore structure tuning, substantial

specific surface area, and the potential for numerous sites facilitating  $\text{Li}^+$  insertion, thereby resulting in elevated theoretical capacities,<sup>19–22</sup> as recent reviews report.<sup>23–25</sup> The high porosity of MOFs offers the advantage of accommodating the significant volume expansion arising from conversion reactions, thereby improving the cyclability of the electrodes compared to TMN materials. However, this high porosity is accompanied by low densities, and MOF electrodes tend to have high gravimetric capacity but reduced volumetric capacity, which is the most critical issue to address.<sup>26</sup> Furthermore, in some cases, MOFs undergo irreversible decomposition or conversion into amorphous phases during lithiation/delithiation unloading processes. The determination of actual active materials, the characterization of amorphous phases and the clarification of the relationship between MOFs and the corresponding active phases after cycling are challenging. Additionally, MOFs typically exhibit reduced electrical conductivity and are usually used in mixtures with highly electrical conductive materials or calcined to obtain structured ordered carbon-based materials.<sup>27</sup>

A family of MOFs accessible through an environmentally friendly procedure is exemplified by  $\text{M}(\text{dca})_2\text{pyz}$ , where M represents a transition metal (TM: Fe, Co, Ni); dca stands for



**Fig. 1** (a) Schematic representation of the crystal structure of the  $\text{M}(\text{dca})_2\text{pyz}$  compounds. For enhanced visualization, the unit cells have been expanded, and the  $[\text{Mn}_6]$  octahedra within the interpenetrated networks are labeled with distinct colors (cyan and red). (b) ATR-FTIR spectra and (c) zoom of the ATR-FTIR spectra in the range in which the  $\alpha$  (blue area) and  $\beta$  (red area) phases can be distinguished<sup>29</sup> of  $\text{Fe}(\text{dca})_2\text{pyz}$  in brown,  $\text{Co}(\text{dca})_2\text{pyz}$  in pink and  $\text{Ni}(\text{dca})_2\text{pyz}$  in blue. (d) Raman spectra of the three MOFs in the region of  $\text{M}^{2+}$  translation dca libration and in-plane dca vibration modes. (Inset) Raman spectra of the three MOFs in the region of  $\text{C}\equiv\text{N}$  stretching modes.



dicyanamide ( $C_2N_3^-$ ); and pyz denotes pyrazine ( $C_4H_4N_2$ ). This method employs water as the only solvent and involves synthesis at low temperatures ( $\leq 80$  °C).<sup>28</sup> These MOFs are reported to present an  $\alpha$  phase consisting of an  $\alpha$ -polonium structure with two interpenetrated 3D  $ReO_3$ -related networks. Bidentate dca ligands act as bridges between TM cations, forming square-grid-like  $M(dca)_2$  sheets, and the pyz ligands link these sheets together, constituting the 3D networks (Fig. 1a). At room temperature, these compounds exhibit an orthorhombic crystal structure with the  $Pnma$  space group, characterized by dynamic disorder of the dca and pyz ligands. This particular structure reduces the porosity of these MOFs, which show a relatively high density ( $\sim 1.7$  mg  $cm^{-3}$ ). To date, the interest in these materials has been focused on their magnetic and electrical properties,<sup>28,29</sup> being studied as a precursor for solar evaporators,<sup>30,31</sup> oxygen reduction and evolution reactions<sup>32,33</sup> or for microwave absorbers.<sup>34</sup> But, as far as the authors are concerned, it has never been studied as an anode in LIBs.

Here, we propose  $M(dca)_2pyz$  ( $M$ : Fe, Co and Ni) as environmentally friendly and electrochemically competitive counterparts to TMNs for LIB anodes. These MOFs are suitable for comparison with TMNs because they are based on N-TM, C-N, C=N, and C $\equiv$ N bonds like the found in TMNs and their derivatives, and also their ligands can potentially enhance electrode performance for LIBs. First, the relatively low energy position of pyz  $\pi^*$  orbital can promote metal-to-ligand back-bonding.<sup>35,36</sup> Second, the  $-C\equiv N$  groups, in dca ligands, are of great interest in cation storage, as suggested by the numerous studies based on Prussian Blue Analog (PBA) materials due to the high theoretical capacity, e.g.  $\sim 400$  mA h  $g^{-1}$  for  $Co_3[Co(CN)_6]_2$ ,<sup>37</sup> and the relatively high discharge potential of 0.7 V vs.  $Li/Li^+$  prevents the formation of metal dendrites. Similar to how coupling PBAs with a conductive substrate can avoid the structure collapse,<sup>38</sup> the integration into the MOF structure can improve cycling stability.<sup>39-42</sup> Third, electron delocalization in dca, induced by interaction between nitrile  $\pi$  electrons and the central nitrogen atom may enhance electron transport among bridged metal centers,<sup>43</sup> particularly in the  $M(dca)_2$  planes potentially improving electronic conductivity, addressing a key limitation of MOFs as LIB electrodes. Last, the structure of two intercalated networks should increase the capacity density of the electrodes because of the higher density of these materials. This study analyzes the performance of  $M(dca)_2pyz$  as LIB electrodes, comparing them to reported TMN studies. It also investigates the influence of the TM center on performance and discusses the lithiation mechanism, providing valuable insights for advancing the design of MOFs as LIB electrodes.

## 2 Materials and methods

### 2.1 Synthesis

Deionized water was the green solvent for all synthesis. All products, purchased from Merck, were used without any further treatment: iron(II) perchlorate hexahydrate  $Fe(ClO_4)_2 \cdot 6H_2O$  (98%), cobalt(II) nitrate hexahydrate  $Co(NO_3)_2 \cdot 6H_2O$  (98%),

nickel(II) nitrate hexahydrate  $Ni(NO_3)_2 \cdot 6H_2O$  (98.5%), sodium dicyanamide  $NaN(CN)_2$  (96%) and pyrazine  $CH_4H_4N_2$  (96%).

For the synthesis, 5 mL of TM ( $M(NO_3)_2 \cdot 6H_2O$ ) and 10 mL of a solution containing 1.2 mmol of  $Na(dca)$  and 0.6 mmol of pyrazine were mixed in warm conditions (Fe 60 °C, Co and Ni 80 °C).<sup>28</sup> Crystals obtained after cooling were washed with ethanol and dried at room temperature. For brevity,  $M(dca)_2pyz$  samples are labelled as Fe-MOF, Co-MOF, and Ni-MOF based on the transition metal used.

### 2.2 Powders characterization

Powder X-Ray Diffraction (PXRD) characterization was performed using an Empyrean diffractometer from Panalytical using Cu  $K\alpha$  radiation ( $\lambda = 1.5406$  Å) and a PIXcel-1D Medipix3 detector between 5 and 45°  $2\theta$  at a scan step of 0.026° and accumulating 200 s. Scanning Electron Microscopy (SEM) images were obtained using a FEG INSPECT 50 from FEI. ATR-FTIR measurements were performed in a PerkinElmer Spectrum 100 instrument between 4000 and 380  $cm^{-1}$  obtaining the media of 8 scans. Raman spectra measurements were carried out using a DILOR XY spectrometer with a CCD detector and 2  $cm^{-1}$  of spectral resolution. An excitation wavelength  $\lambda = 568.2$  nm from a krypton-argon laser (Melles Griot, Carlsbad, CA, USA) was used with an Olympus BH-2 microscope and a  $\times 50$  objective, collecting the Raman signal with backscattering geometry. The output source power was always kept at a minimum, checking that no damage was induced in the sample. Thermogravimetric analysis (TGA) measurements were performed in SDT 2960 from TA Instruments from room temperature to 600 °C at a rate of 5 °C  $min^{-1}$  in a  $N_2$  atmosphere. The electronic conductivity ( $\sigma$ ) was obtained by measuring the resistance ( $R$ ) of the MOF powders between the two stainless steel current collectors ( $\varnothing$  7 mm) in a Swagelok cell. A pressure of 226 MPa was applied using a hydraulic press (RIKEN SEIKI P-163).  $R$  was obtained by fitting a Randles model equivalent circuit to the electrochemical impedance spectroscopy (EIS) data measured applying 1 V between  $10^6$  to  $10^{-2}$  Hz, performed in an Autolab M204.<sup>44</sup> The thickness ( $l$ ) of the final pellet was measured using a micrometer (Mitutoyo). The electronic conductivity ( $\sigma$ ) was then calculated using the equation  $\sigma = l/(R \cdot A)$ , where  $A$  is the area of the pellet.

### 2.3 Electrochemical characterization

$M(dca)_2pyz$ : carbon black Super P (99+, AlfaAesar); poly(vinylidene fluoride) (PVDF, AlfaAesar) were mixed in an agate mortar and pestle in a weight ratio 80 : 15 : 5 using *N*-methyl pyrrolidone (NMP, Sigma-Aldrich) as the solvent. The slurry was cast on a copper foil (thickness 0.025 mm, 99.8%, Thermo-Scientific) and heated first in a hot plate for 10 minutes to rapidly remove the solvent and to avoid particle segregation and then in a thermostatic vacuum dryer (Selecta) at 120 °C in vacuum conditions for 12 hours to assure NMP removal. After applying 128 kg  $cm^{-2}$  of pressure on the copper foil with the sample, the discs electrodes of 8 mm in diameter were cut and assembled in either a CR2032 coin cell (for electrochemical measurements) or Swagelok cells (for characterizing electrodes





after cycling) inside an Ar glovebox (VAC-ATM). Lithium foil (thickness 1.5 mm, Sigma-Aldrich) was used as the reference and counter electrode, and the electrolyte employed was 1 M LiPF<sub>6</sub> in EC : DEC (ethylene carbonate : diethyl carbonate 1 : 1) (v/v) solution (Sigma-Aldrich) embedded in a fiber glass (Grade GF/C, Whatman® glass) separator. The average active material loading in the electrodes was  $1.2 \pm 0.4 \text{ mg cm}^{-2}$  for Fe(dca)<sub>2</sub>pyz,  $3.0 \pm 0.9 \text{ mg cm}^{-2}$  in the case of Co(dca)<sub>2</sub>pyz and  $1.7 \pm 0.3 \text{ mg cm}^{-2}$  for Ni(dca)<sub>2</sub>pyz.

A Neware Battery Tester System performed the rate capability and the cycling performance at 200 mA g<sup>-1</sup> tests in the potential range from 0.1 to 3 V vs. Li/Li<sup>+</sup>. Before measuring the cyclability at 200 mA g<sup>-1</sup>, 10 conditioning cycles were performed at 50 mA g<sup>-1</sup> between 0.1 to 3 V vs. Li/Li<sup>+</sup> to develop a stable Solid Electrolyte Interface (SEI). An Autolab M204 was used for doing the cyclic voltammetry measurements (CVs) between 0.1 to 3.4 V vs. Li/Li<sup>+</sup> at 0.1 mV s<sup>-1</sup> and the electrochemical impedance spectroscopy (EIS) between 1 MHz and 1 mHz. Fit data using the proposed equivalent electrical circuit model were obtained with Z-View software.

## 2.4 Electrodes characterization

Electrodes cycled for 5 to 10 lithiation/delithiation cycles in Swagelok cells and stopped at 0.1 V or 3 V were washed with DEC, dried, and characterized by PXRD and ATR-IR. For XPS and Transmission Electron Microscopy (TEM) measurements, samples were scratched from copper current collectors post-drying. The resulting powders were homogenized in an agate mortar and pestle to characterize the entire sample, reducing the effect of the SEI-present surface. Freshly prepared electrodes were also measured using the same techniques.

PXRD measurements of the electrodes were performed on a PANalytical Empyrean diffractometer between 5 and 45° 2θ using a scan step of 0.026°. ATR-FTIR measurements were performed on a Bruker FTIR Vertex 70 instrument between 4000 and 600 cm<sup>-1</sup> obtaining the media of 40 scans. XPS measurements were performed on a X-ray Photoelectron Spectroscopy AXIS Supra™ from Kratos with monochromated Al Kα = 1486.6 eV. The software CasaXPS was used for analyzing the spectra and the calibration was done considering the maximum of the C 1s high resolution peak at 284.8 eV. Transmission electron microscopy analyses were carried out in a TITAN FEI XFEG 60-300 microscope, operated at 300 kV, equipped with a monochromator, a CEOS spherical aberration corrector for the electron probe, a Gatan Tridiem Energy Filter (GIF) and an Oxford EDX spectrometer for chemical analyses. Prior the experiments the aberrations were reduced using a gold standard sample assuring a spatial resolution of 0.8 Å. The materials were dispersed in absolute ethanol and few drops of the suspension were placed onto holey carbon copper grids.

## 3 Results and discussion

### 3.1 Powders characterization

PXRD patterns at room temperature of the three M(dca)<sub>2</sub>pyz compounds indicate that they are in a single-phase state, as

indicated by the comparison with the simulated single crystal X-ray diffraction data (SCXRD) (Fig. S1†) and consistent with literature.<sup>28,29</sup> SEM images (Fig. S2†) show that Fe-MOF is formed by big stacked sheets surrounded by small rounded particles of the size from nanometers up to 2 μm and Co-MOF is structured as stacked sheets that form needle-like structures. Conversely, Ni-MOF exhibits a ball-like structure formed by needles. The interpenetrated networks of these MOFs reduce notably the porosity of these materials (Fig. S3†), with estimated surface areas of 3 m<sup>2</sup> g<sup>-1</sup>, 2 m<sup>2</sup> g<sup>-1</sup>, and 10 m<sup>2</sup> g<sup>-1</sup> for Ni(dca)<sub>2</sub>pyz, Co(dca)<sub>2</sub>pyz, and Ni(dca)<sub>2</sub>pyz, respectively.

The ATR-FTIR spectra (Fig. 1b) are also in agreement with the literature,<sup>29</sup> displaying all the characteristic bands for Co-MOF and Ni-MOF. However, Fe-MOF spectrum shows two additional bands at ~3280 and ~1594 cm<sup>-1</sup>, attributable to O–H stretching and bending vibrations from H<sub>2</sub>O intercalated into the MOF structure,<sup>40–42</sup> confirmed by TGA analysis (Fig. S4†). Only Fe-MOF shows a slight mass loss from room temperature to 150 °C and a second mass loss from 160 °C to 200 °C, attributed to the loss of superficial and interstitial water, respectively.<sup>40–42,45</sup> The second weight loss converges with a third that ends at 270 °C, similar to Co-MOF (220–270 °C) and at lower temperature than Ni-MOF (300–350 °C), suggesting stronger Ni–N interaction. This weight loss is associated to the removal of pyz ligands. Subsequently, a gradual weight loss at higher temperatures occurs due to the partial loss of dca ligands.<sup>28</sup>

Fig. 1c shows a close-up view of the ATR-FTIR spectra of the region that can be used to distinguish between the α (blue area) and the β (red area) phases.<sup>29</sup> Co-MOF and Ni-MOF exhibit no discernible contributions for the β phase, indicating exclusive α phase presence. However, in Fe-MOF, a shoulder appears at ~1335 cm<sup>-1</sup>. This peak is assigned to the β phase, characterized by each metallic center being linked to two others through two pairs of dca ligands, resulting in 1D chains joined by pyz molecules forming interlocked 2D layers. Despite the absence of this phase in the PXRD spectrum, the detection of H<sub>2</sub>O molecules suggests that some Fe atoms may adopt this β phase, coordinating with two dca ligands, two H<sub>2</sub>O molecules, and two pyz ligands. These dca ligands link to water molecules *via* the uncoordinated nitrile nitrogen, giving double dca··H<sub>2</sub>O bridges between the Fe atoms in adjacent chains. This structural arrangement aligns with a previous reported Fe(dca)<sub>2</sub>(-bipy) MOF with two 3D interpenetrating α-Po related hydrogen bond network.<sup>46</sup>

Fig. 1d shows the Raman spectra of the three samples in different regions of Raman shift. Fe-MOF presents inhomogeneous crystallinity, with well-defined and polarized crystals embedded in an amorphous matrix, corresponding the spectrum showed in Fig. 1d to the former regions. Besides, Fe-MOF turned out to be much more sensitive to radiation than their Ni and Co counterparts and a lower excitation power was needed in order to avoid its decomposition. Co-MOF was fully composed of elongated microcrystals whose transparency made it necessary to carry out the measurements in absolute darkness to avoid parasitic signals. Ni-MOF forms spherical crystals, resulting in no polarization of the signal. The bands observed in



Table 1 Electronic conductivity of the MOFs, calculated from EIS spectra in Fig. S6

	Fe(dca) <sub>2</sub> pyz	Co(dca) <sub>2</sub> pyz	Ni(dca) <sub>2</sub> pyz
$\sigma$ (S cm <sup>-1</sup> )	$3.47 \times 10^{-7}$	$1.11 \times 10^{-8}$	$1.05 \times 10^{-8}$

low energy spectra are compatible with results from literature,<sup>47,48</sup> where the region below 300 cm<sup>-1</sup> is ascribed to lattice modes mainly from M<sup>2+</sup> translations, together with some contribution from translations and librations modes of dca. Co-MOF and Ni-MOF show similar spectra while Fe-MOF spectrum might highlight a distinct chemical environment on Fe atoms. The band in the 600–650 cm<sup>-1</sup> region can be assigned to the in-plane CNC bending mode, while the 2250 cm<sup>-1</sup> region would correspond to the C≡N stretching modes of dca ligand, showing an increase in wavenumber from Fe to Co to Ni, as expected from the larger force constant between C and N.<sup>28</sup> A

weak band (not shown) corresponding to the C–N symmetric stretching mode was observed around 940 cm<sup>-1</sup>. The region where the main peaks related to pyrazine moiety is represented in Fig. S5.† The spectra suggest that Ni-pyz interaction is stronger than in Co-pyz and particularly than Fe-pyz.

These MOFs exhibit electrical conductivities (Table 1) of 3/2 orders of magnitude higher than most MOFs, where the electronic conductivity typically falls below 10<sup>-10</sup> S cm<sup>-1</sup>.<sup>49</sup> Although the electrical conductivity is low, the substantial increase by several orders of magnitude is significant for studying these materials as battery electrodes. In addition, this property becomes less critical the smaller the particle size.

### 3.2 Electrochemical performance

Fig. 2a shows the specific capacity of the three MOFs at different applied currents. It is expressed with respect to the total mass of the electrode considering the contribution of carbon black (Fig. S7†) that it is not negligible, especially for Ni-MOF. The

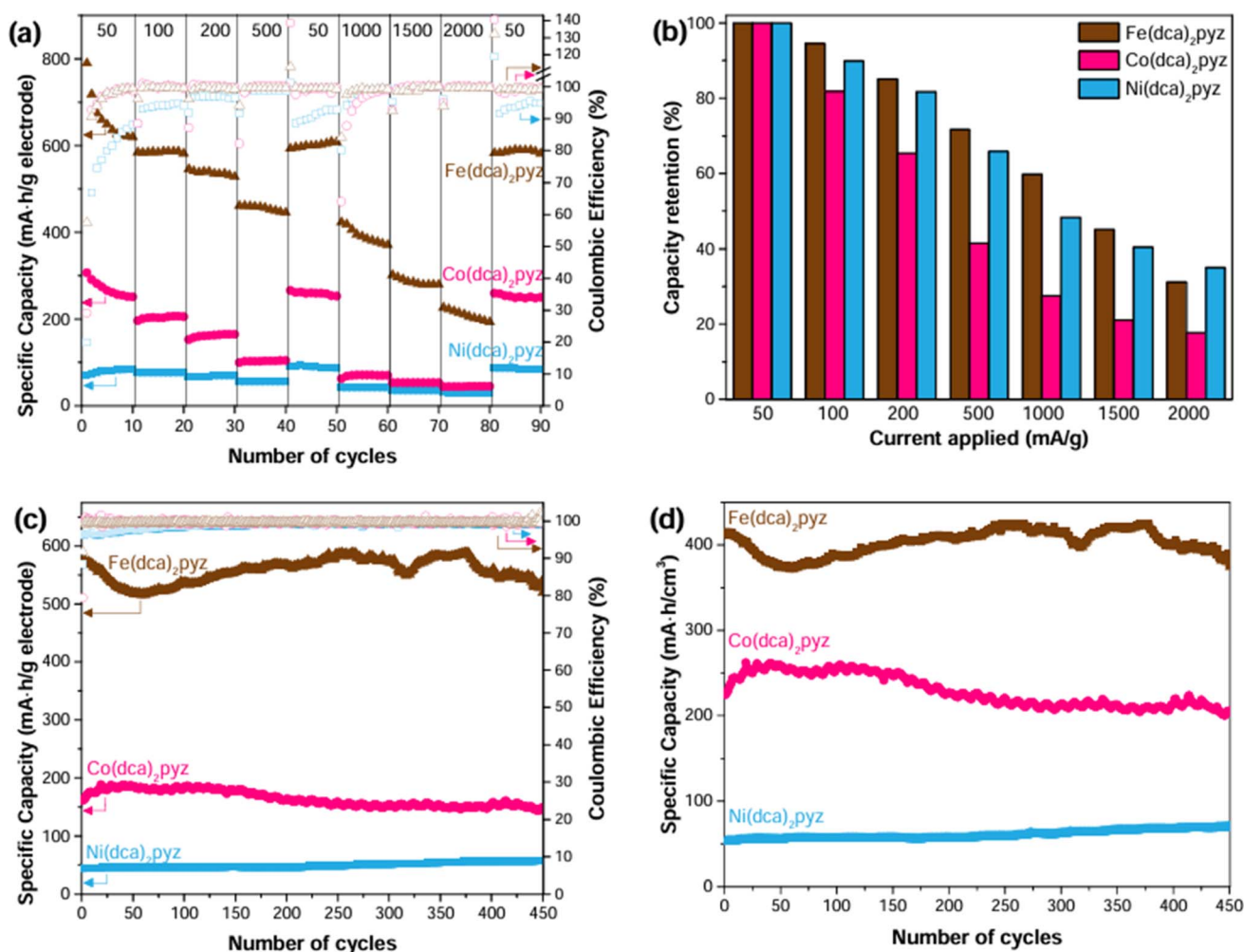


Fig. 2 Delithiation specific capacities (filled symbols) and coulombic efficiencies (hollow symbols) of Fe(dca)<sub>2</sub>pyz (brown), Co(dca)<sub>2</sub>pyz (pink) and Ni(dca)<sub>2</sub>pyz (blue) showing (a) the rate capability and (c) the cycling performance at 200 mA g<sup>-1</sup>. The numbers inside the graph indicate the current applied as mA h g<sup>-1</sup> MOF. (b) Capacity retention of the rate capability test with respect to the value obtained in the tenth lithiation/delithiation cycle at 50 mA g<sup>-1</sup>. (d) Cycling performance graph shown in (c) expressing the values of delithiation specific capacities as mA h cm<sup>-3</sup> electrode.



analysis of the first cycle capacities and the evolution of the coulombic efficiencies can be found in Fig. S8.† Fe-MOF presents the highest values of specific capacity at all measured lithiation/delithiation rates, followed by Co-MOF and Ni-MOF. In Fe-MOF, there is an initial decrease in capacity during the first 10 cycles at 50 mA g<sup>-1</sup>, mainly due to solid electrolyte interface (SEI) formation. However, the capacity stabilizes approximately at 586 mA h g<sup>-1</sup> when the rate increases to 100 mA g<sup>-1</sup>. At higher applied currents, capacities show a slight decline, particularly at rates surpassing 1000 mA g<sup>-1</sup>, and recovers upon returning to low rates. This recovery suggests limiting kinetic factors rather than degradation phenomena. In Co-MOF, the descending tendency is observed only in the initial 10 cycles, attributed to SEI formation, while in Ni-MOF, the specific capacity increases from the first cycle.

To assess the rate capability of these materials, Fig. 2b calculates their capacity retention with respect to that obtained in the tenth cycle at 50 mA g<sup>-1</sup>. Fe-MOF electrode maintains the highest percentage of capacity retention up to 1500 mA g<sup>-1</sup>, probably due to its higher electronic conductivity (Table 1). Ni-MOF retains more capacity at each rate than Co-MOF, despite having similar conductivities. This could be ascribed to the smaller crystal size of Ni-MOF, resulting in a shorter path for electrons travel. Thus, size reduction and electrical conductivity enhancement increase capacity retention in the MOFs studied under faster charge/discharge rates.

Cycling tests demonstrate good cyclability of all three MOFs over 450 cycles (Fig. 2c). After an initial drop in capacity, Fe-MOF capacity increases to a maximum value of 590 mA h g<sup>-1</sup> at cycle 250. Co-MOF shows a gradual increase in capacity from ~160 to ~190 mA h g<sup>-1</sup> in the initial cycles. These increments are likely due to the adsorption of Li<sup>+</sup> as the electrolyte penetrates the internal structure of the MOFs.<sup>19</sup> Subsequently, the specific capacities fluctuate around 550 mA h g<sup>-1</sup> for Fe-MOF and 148 mA h g<sup>-1</sup> for Co-MOF, representing a capacity retention of 90% (87%) and 92% (79%) relative to the initial (maximum) value. Further cycling of Co-MOF reveals a continued descending trend, reaching 118 mA h g<sup>-1</sup> after 1000 cycles, equivalent to 73% (63%) of the initial (maximum) value (Fig. S9a†). In contrast, Ni-MOF electrode exhibits a continuous increase in specific capacity from 44 mA h g<sup>-1</sup> to 57 mA h g<sup>-1</sup> at cycle 450 and continues to increase up to 75 mA h g<sup>-1</sup> after 1000 cycles (Fig. S9b†).

Up to now, the specific structure of two interpenetrating networks does not seem to reduce the cyclability of these electrodes, which demonstrate high capacity retention. Notably, this structure results in MOFs with relatively high densities (1.77 g cm<sup>-3</sup>, 1.65 g cm<sup>-3</sup>, and 1.70 g cm<sup>-3</sup> for Co(dca)<sub>2</sub>pyz, Fe(dca)<sub>2</sub>pyz and Ni(dca)<sub>2</sub>pyz, respectively), comparable to TMNs and approximately more than two times higher than typical porous MOFs. Consequently, these MOFs exhibit competitive volumetric capacities, akin to inorganic materials such as LiCoO<sub>2</sub> or LiFePO<sub>4</sub>,<sup>50</sup> and particularly high for MOFs.<sup>26</sup> Fig. 2d shows the volumetric capacity of the three studied MOFs: the Fe-MOF around 400 mA h cm<sup>-3</sup>, the Ni-MOF shows a low value of 50 mA h cm<sup>-3</sup>, and the Co-MOF has an intermediate value of 250 mA h cm<sup>-3</sup>.

Table S1† compares the results obtained for M(dca)<sub>2</sub>pyz in this study with some results reported for TMNs. Typically, in literature values of specific capacity do not consider the contribution of the conductive additive. To facilitate the comparison, the specific capacities obtained here are recalculated based on the mass of MOF, as mA h g<sup>-1</sup> MOF. The recalculated values for Fe, Co and Ni compounds after 450 cycles at 200 mA h g<sup>-1</sup> are 650, 185 and 72 mA h g<sup>-1</sup>, respectively. Fe(dca)<sub>2</sub>pyz demonstrates similar or even better performance than TMNs, suggesting its potential as a green alternative to obtain iron nitride derivatives as electrodes. Nevertheless, Co(dca)<sub>2</sub>pyz and Ni(dca)<sub>2</sub>pyz show lower specific capacities than reported values, indicating their poor performance as LIB anodes compared to TMNs, particularly Ni-MOF. Compared to MOFs used as anodes for LIBs,<sup>23,25</sup> Fe(dca)<sub>2</sub>pyz shows competitive values considering that the studied voltage window is between 0.1 V and 3 V vs. Li/Li<sup>+</sup> and higher energy density is expected under more optimized conditions, such as increasing the voltage window up to 0.01 V vs. Li/Li<sup>+</sup>, increasing the amount of carbon black additive or further electrode structuring. More details are provided in Table S2.†

### 3.3 Effect of the TM in the electrochemical performance

The previous section shows important differences in the performance of the three compounds as electrodes for LIBs (specific capacity and rate capability) despite having the same unit formula and similar structural nature. For instance, the number of intercalated/reacted Li<sup>+</sup> per Fe(dca)<sub>2</sub>pyz, Co(dca)<sub>2</sub>pyz and Ni(dca)<sub>2</sub>pyz molecule is 7, 2.5 and 0.5, respectively, at 50 mA g<sup>-1</sup> (after subtracting the contribution of carbon black).

To study these distinctions, Fig. 3 presents PXRD diffractograms of both pristine and cycled electrodes terminated at 0.1 V (lithiated) and 3 V (delithiated) for the three MOFs. The crystalline structure of the MOF powders (Fig. S1†) is preserved in the non-cycled (fresh) electrodes. However, cycled electrodes of Fe-MOF and Co-MOF lack the initial peaks observed in fresh electrodes, indicating either a reduction in MOF crystal domain or the formation of an amorphous structure.<sup>51</sup> Lithiated Fe-MOF exhibits only four discernible diffraction peaks at 5.54°, 20.25°, 32.70°, and 36°. The one at lower angles could be attributed to a small contribution of the low-temperature crystal structure of this compound family (Fig. 3d), featuring a monoclinic structure with ordered ligands in space group *P2<sub>1</sub>/n*.<sup>28,29</sup> The second peak is attributed to Li<sub>2</sub>CO<sub>3</sub> from the SEI,<sup>10</sup> while the latter two peaks could be assigned to Fe<sub>2</sub>O<sub>3</sub> due to the oxidation of iron metal particles exposed to the atmosphere.<sup>39</sup> This loss of crystallinity and the appearance of Fe<sub>2</sub>O<sub>3</sub> peaks align well with a conversion and displacement reaction.<sup>39</sup> The same PXRD pattern is observed for the delithiated Fe electrode, with the first peak being more intense and slightly displaced (5.51°), indicating a possible preference for this crystalline structure during the delithiation process. Co-MOF also exhibits a small peak at 20.25° at 0.1 V, attributed to Li<sub>2</sub>CO<sub>3</sub> from SEI, and a peak at 32.56°, likely related to the formation of Co(OH)<sub>2</sub> during sample exposure to the atmosphere. At 3 V, the SEI-associated peak disappears, and two new peaks emerge at 5.54° and 9.45° that



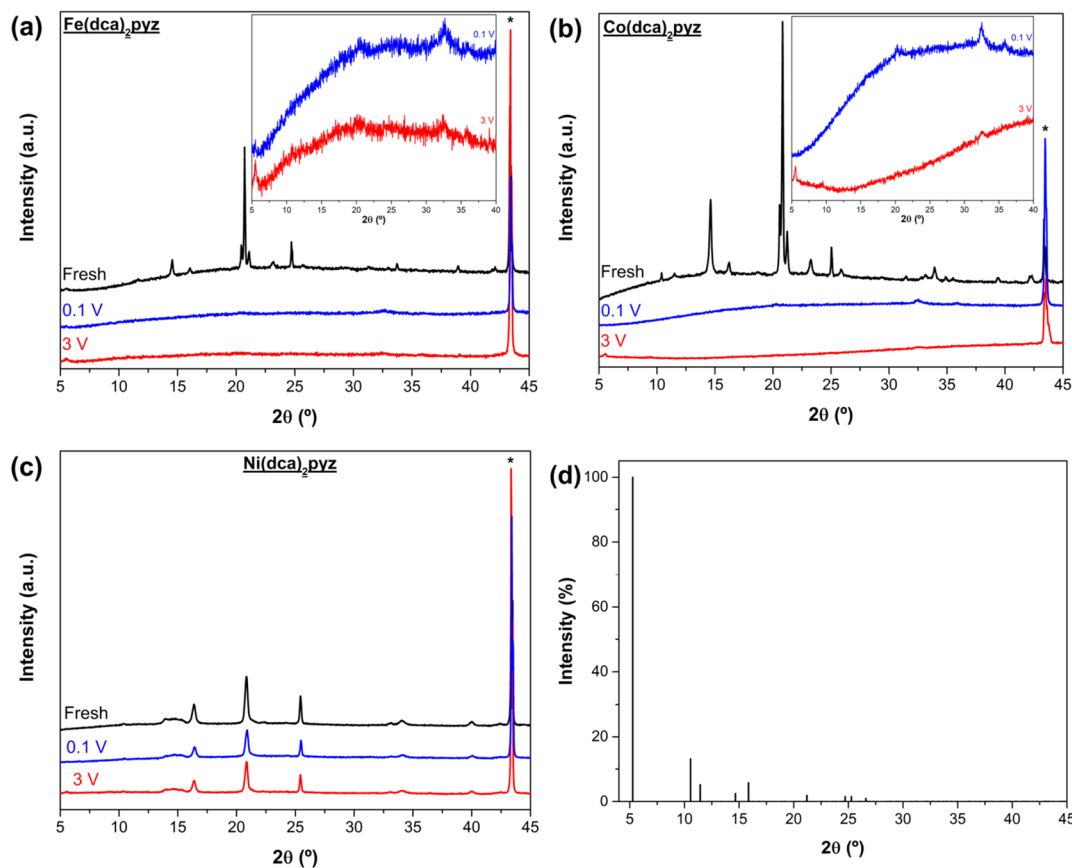


Fig. 3 PXRD of the electrodes before (black) and after cycling them and stopped at 0.1 V (blue) and 3 V (red) of (a)  $\text{Fe}(\text{dca})_2\text{pyz}$ , (b)  $\text{Co}(\text{dca})_2\text{pyz}$  and (c)  $\text{Ni}(\text{dca})_2\text{pyz}$ . Insets in (a) and (b) show magnified patterns of the lithiated and delithiated electrodes for visualizing the small peaks present. Asterisks indicate the peak attributed to copper from the current collector. (d)  $hkl$  plot of the low temperature monoclinic crystal structure of  $\text{M}(\text{dca})_2\text{pyz}$  family of MOFs.

can be related with the formation of the monoclinic crystal structure. In contrast, Ni-MOF retains its crystallinity post-cycling, favored by the lower amount of  $\text{Li}^+$  introduced during the lithiation process. However, a small peak appears at  $5.54^\circ$  in the delithiated electrode, indicating a possible formation of the ordered monoclinic structure during the delithiation process – a phenomenon common to all three MOFs. These findings illustrate that the electrodes with high specific energy density are the result of amorphizing the original MOFs. Consequently, the resulting materials, which can be identified as amorphous organometallic (AMO) compounds, effectively function as anodes.

XPS spectra (Fig. 4) reveal notable changes in N and metal node environments in pristine and cycled electrodes at 0.1 and 3 V. High-resolution N 1s spectra of the three fresh electrodes can be convolved into three peaks. The peak at  $\sim 399$  eV is assigned to the nitrile N  $\text{sp}$  hybridization. The N  $\text{sp}^2$  hybridization band can convolve into two peaks at 400 eV and 400.5 eV corresponding to the N of the pyz and dca, respectively, since in the first case the N coordinates with the TM according to the MOF structure. After cycling, the N 1s spectra show an important shift to lower B.E., in which the new peak at  $\sim 398.0$  eV is plausibly attributed to reduced N bonding  $\text{Li}^+$ , confirming the

active involvement of the N atom in the storage process. The broad band of the Fe-MOF indicates different chemical environments of the N in this MOF that may correspond to the amorphous material formed. The small differences between the spectra obtained for the electrodes stopped at 0.1 V and 3 V suggest that the initial MOF is not recovered, like it is observed in conversion inorganic electrodes.<sup>52</sup> The spectra in cycled Co-MOF show the main peak at  $\sim 398.2$  eV with a broad tail at higher energies, suggesting high negative charges accumulated on the N and a different  $\text{Li}^+$  accumulation mechanism than in Fe-MOF. In this case, there is a slight shift to higher energies at 3 V respect to 0.1 V. This shift is most noticeable in Ni-MOF, which is the only electrode that does not amorphize in cycling process, and indicates the accumulation and drain of negative charges as a function of the voltage at which the batteries were stopped. Regarding metal node centers, fresh samples exhibit a mixed oxidation state (+2/+3) of the metal nodes, attributed to enhanced backbonding from the metal to the N pyrazine, influenced by its relatively low position of the  $\pi^*$  orbital.<sup>35,36</sup> Lithiated Fe-MOF reveals the presence of  $\text{Fe}^0$  which confirms the conversion reaction mechanism during lithiation process. However, this mechanism does not appear to be the only one, as not all Fe units undergo reduction, and both  $\text{Fe}^{2+}$  and  $\text{Fe}^{3+}$





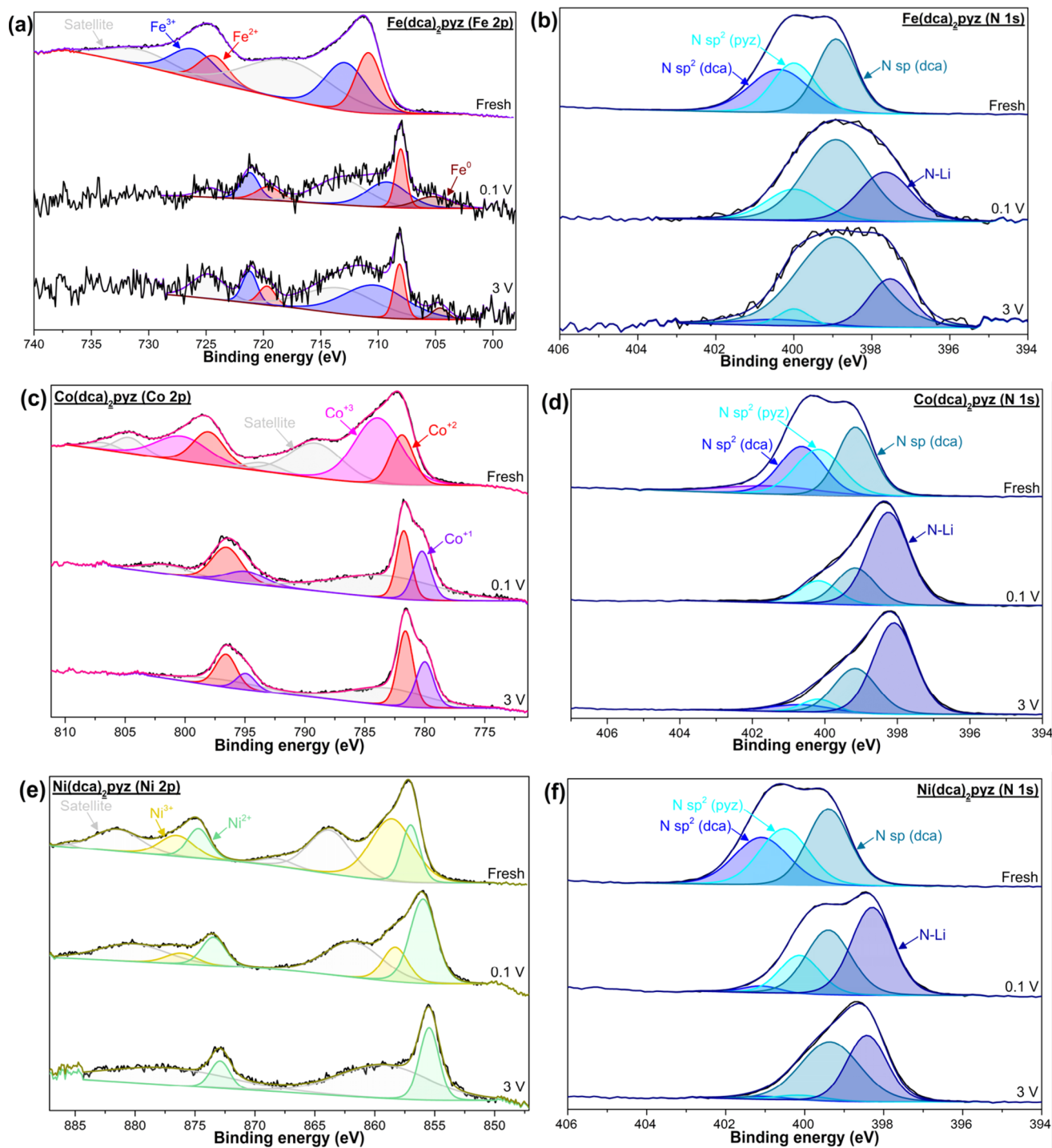


Fig. 4 XPS high resolution M 2p spectra of (a) Fe(dca)<sub>2</sub>pyz, (c) Co(dca)<sub>2</sub>pyz and (e) Ni(dca)<sub>2</sub>pyz, and N 1s spectra of (b) Fe(dca)<sub>2</sub>pyz, (d) Co(dca)<sub>2</sub>pyz and (f) Ni(dca)<sub>2</sub>pyz of freshly prepared (pristine), lithiated (0.1 V) and delithiated (3 V) electrodes.

remain detectable (although some oxidation during the preparation of the samples on the XPS support in air cannot be completely excluded) and the observation of Fe<sup>0</sup> in the delithiated sample. In contrast, the peak assigned to Co<sup>3+</sup> disappears in the Co-MOF cycled electrodes and a lower energy peak appears in the spectra, which can be assigned to Co<sup>1+</sup> or Co<sup>0</sup>. In this case, TEM characterization with EELS (discussed below) and the lower capacity of the battery formed with Co-MOF

compared to Fe-MOF rule out the conversion mechanism and Co<sup>0</sup> formation. Ni-MOF exhibits a contrasting behavior, with the observation of Ni<sup>3+</sup> at 0.1 V, which disappears at 3 V. This behavior suggests that the process of injecting negative charges to the MOF during the lithiation step is in part obstructed by the oxidation of Ni nodes,<sup>53</sup> hindering Li<sup>+</sup> intercalation.

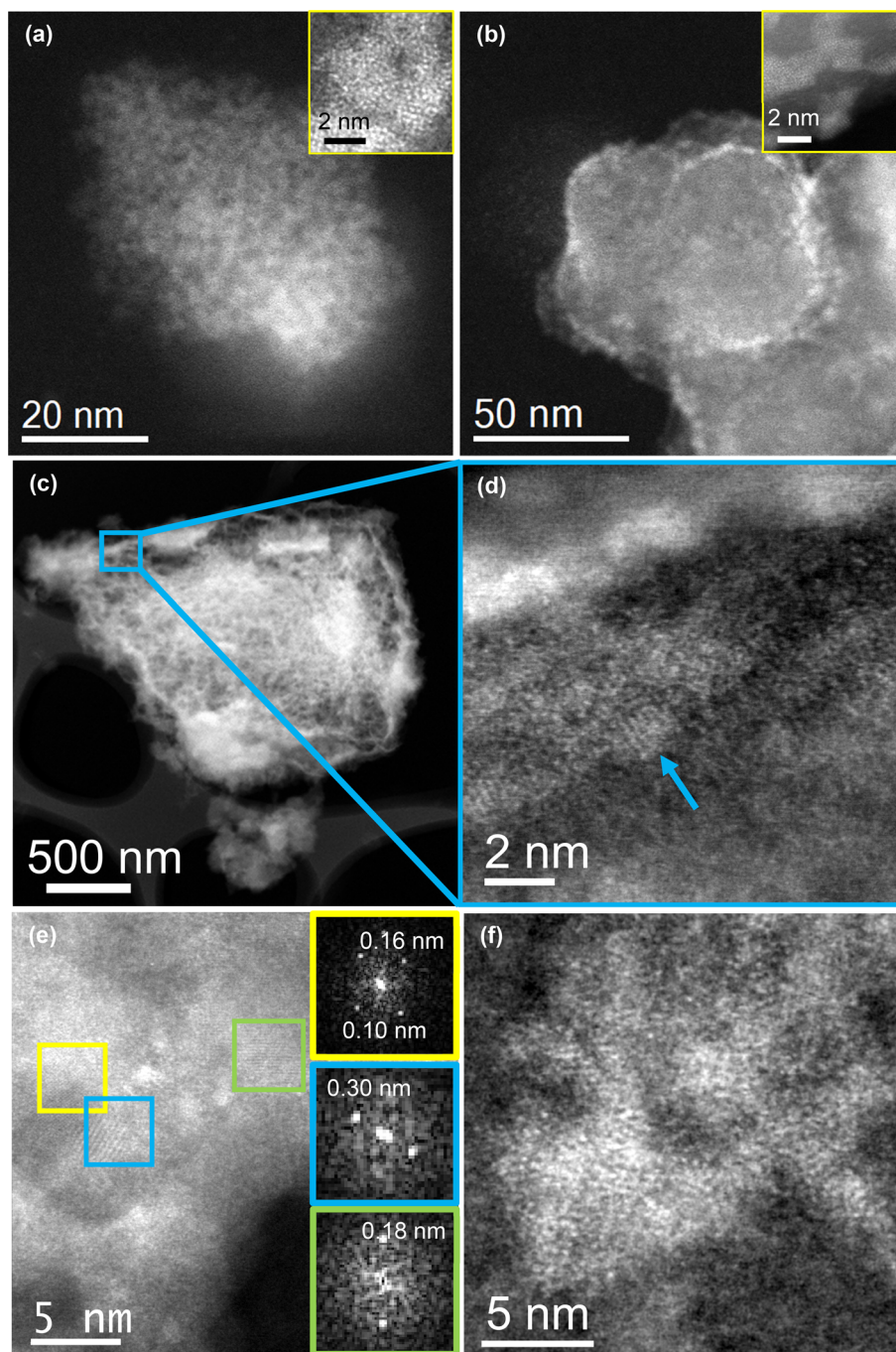
The presence of Fe<sup>0</sup> together with the cationic form and Ni and Co only in the cationic form in lithiated electrodes is





confirmed by spherical aberration corrected (Cs-corrected) Scanning TEM (STEM) combined with an annular dark field detector (ADF) and EELS (Fig. 5). Lithiated Fe-MOF shows the presence of Fe in two distinct forms: dispersed as nanoparticles/clusters (Fig. 5a) and attached to the MOF particles (Fig. 5b). Atomic-resolution data (inset Fig. 5a and b) highlight a partial crystallization in both scenarios, especially for those particles

over the MOF. Despite oxygen was found in both types of clusters (see EELS from Fig. S10a and b†) the low oxygen content in those separated from the MOF indicates that these Fe would predominantly be in  $\text{Fe}^0$  state. Similar findings were observed for lithiated Co-MOF, but Co is consistently associated with the MOF particles (Fig. 5c). A low-magnification Cs-corrected STEM-ADF image in Fig. 5c displays a couple of MOF particles whose



**Fig. 5** Cs-corrected STEM-HAADF analysis for the three MOFs. (a) and (b) Analysis for  $\text{Fe}(\text{dca})_2\text{pyz}$ , including atomic resolution data of the two types of Fe observed (a) isolated and (b) with the MOF. The closer visualization of the structure is shown on the inset. (c) Low-magnification image of a  $\text{Co}(\text{dca})_2\text{pyz}$  MOF particle with the metal on top. (d) Magnified image from the blue square marked in (c). (e) High-magnification image of  $\text{Ni}(\text{dca})_2\text{pyz}$  with different crystallite domains, denoted by colored squares. Their correspondent (same color code) FFTs are also displayed. (f) High-magnification image of another region of  $\text{Ni}(\text{dca})_2\text{pyz}$  showing that the metal is not crystallized.



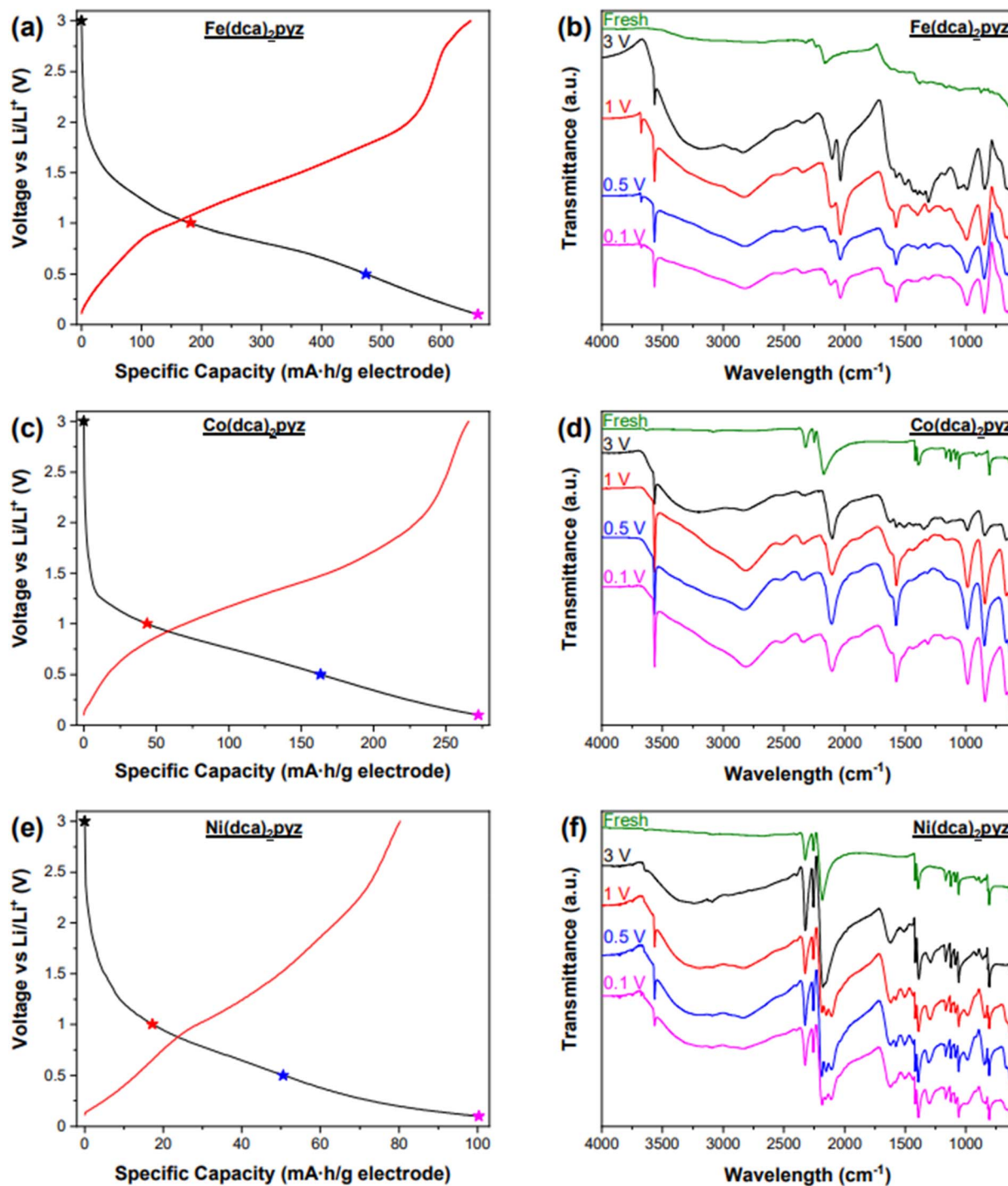


Fig. 6 Galvanostatic lithiation (black) – delithiation (red) profiles of (a) Fe(dca)<sub>2</sub>pyz, (c) Co(dca)<sub>2</sub>pyz and (e) Ni(dca)<sub>2</sub>pyz marking with a star the voltages in which the electrodes were stopped to be measured by ATR-FTIR. The results of these measurements are shown in (b) for Fe(dca)<sub>2</sub>pyz, (d) for Co(dca)<sub>2</sub>pyz and (f) for Ni(dca)<sub>2</sub>pyz.

surface is covered by the metal. A closer inspection of the structure of the material (Fig. 5d) reveals that Co was also in the form of clusters where only small domains were partially crystallized (blue arrow). The measured *d*-spacing of 2.42 Å did not align with any values for Co<sup>0</sup>, suggesting, at least, partial oxidation of the metal. The presence of oxygen and cobalt was verified by EELS (Fig. S10c<sup>†</sup>), where both edges are distinctly

identified. Similar results were obtained for lithiated Ni-MOF. After cycling, the metal is predominantly associated with MOF particles, showing partial crystallization in some cases, and forming metal clusters lacking structural order in others (Fig. 5e and f). The distance 0.18 nm can be assigned to *d*<sub>200</sub> of NiO, and 0.16 nm and 0.10 nm to the planes *d*<sub>200</sub> and *d*<sub>222</sub> of Ni, respectively. The FFT of different regions, marked by colored



rectangles are displayed on the inset of Fig. 5e. The fact that none of the  $d$ -spacing measured matched with the  $\text{Ni}^0$ , suggests at least partial oxidation.

To obtain further insight on the lithiation mechanism, ATR-FTIR measurements were performed on fresh and cycled electrodes stopped at different voltages indicated in the galvanostatic charge–discharge plots (Fig. 6). These plots do not show any clear plateau but regions with different slopes, indicating that these materials have a pseudocapacitive behavior, with multi-step processes. Clear differentiation between regions can be observed in the CV graphs, discussed in Fig. S11.† Three regions can be observed in the Fe-MOF, while the slope changes are subtler for Co-MOF and Ni-MOF. In the Fe-MOF: in the first region, from 3 V to  $\sim 1$  V it is estimated that two  $\text{Li}^+$  are inserted, then the slope of the curve decreases to  $\sim 0.5$  V with the estimation that three  $\text{Li}^+$  are inserted, and finally a third section is observed in which two electrons are involved. Based on this Fe-MOF plot, the voltages chosen to stop the batteries and measure the electrodes are 3 V, 1 V, 0.5 V and 0.1 V.

ATR-FTIR of cycled Fe-MOF electrodes present two sharp peaks at  $3678\text{ cm}^{-1}$  (not observed in the sample stopped at 3 V) and  $3566\text{ cm}^{-1}$  that could be assigned to the stretching vibration of non-hydrogen bonded O–H.<sup>54</sup> The absence of a broad band in the region of  $3200\text{--}3600\text{ cm}^{-1}$  on cycled electrodes below 3 V, seems to indicate that these bands correspond to

$\text{LiOH}$  and  $\text{LiOH}\cdot\text{H}_2\text{O}$  respectively,<sup>54,55</sup> probably formed due to samples exposure to the atmosphere during measurements. Cycled Co-MOF and Ni-MOF just present the peak at  $3566\text{ cm}^{-1}$ , but in the case of Ni-MOF, a broad band at  $\sim 3300\text{ cm}^{-1}$  appears at all voltages, so this sharp peak could also be produced by  $\text{H}_2\text{O}$  adsorbed on the surface of the electrode.<sup>56</sup>

$\text{C}\equiv\text{N}$  bands are very sensitive to nitriles chemical environment and they undergo a blue-shift when the atom they are coordinated to is oxidized.<sup>44,57</sup>  $\nu_s(\text{C}\equiv\text{N})$  band shows a red-shift for the cycled Fe-MOF and Co-MOF electrodes not observed for Ni-MOF. This red-shift is plausibly attributed to an injection of the TM charge to the dca ligand, in agreement with the reduction state observed for these two TMs. Besides, in the Fe-MOF is observed a split of the band that has been attributed to the presence of both coordinated and free  $[\text{N}(\text{CN})_2]^-$  ions, which is red-shifted in relation to coordinated ions.<sup>58</sup> In Ni-MOF, the band changes at voltages  $\leq 1$  V, with the split of 3 bands that suggests the loss of symmetry indicating that this functional group starts to participate at lower voltages than in the other two MOFs. Ni-MOF also shows different behavior with the band at  $\sim 1550\text{ cm}^{-1}$ , which appears in the spectra of all the cycled electrodes while this peak is observed in Fe-MOF and Co-MOF when the voltage is  $\leq 1$  V. This band can be assigned to  $\text{C}=\text{N}$  bond, and measured once the zwitterion in pyrazine and/or dicyanamide ligands is broken due to the interaction with  $\text{Li}^+$ .

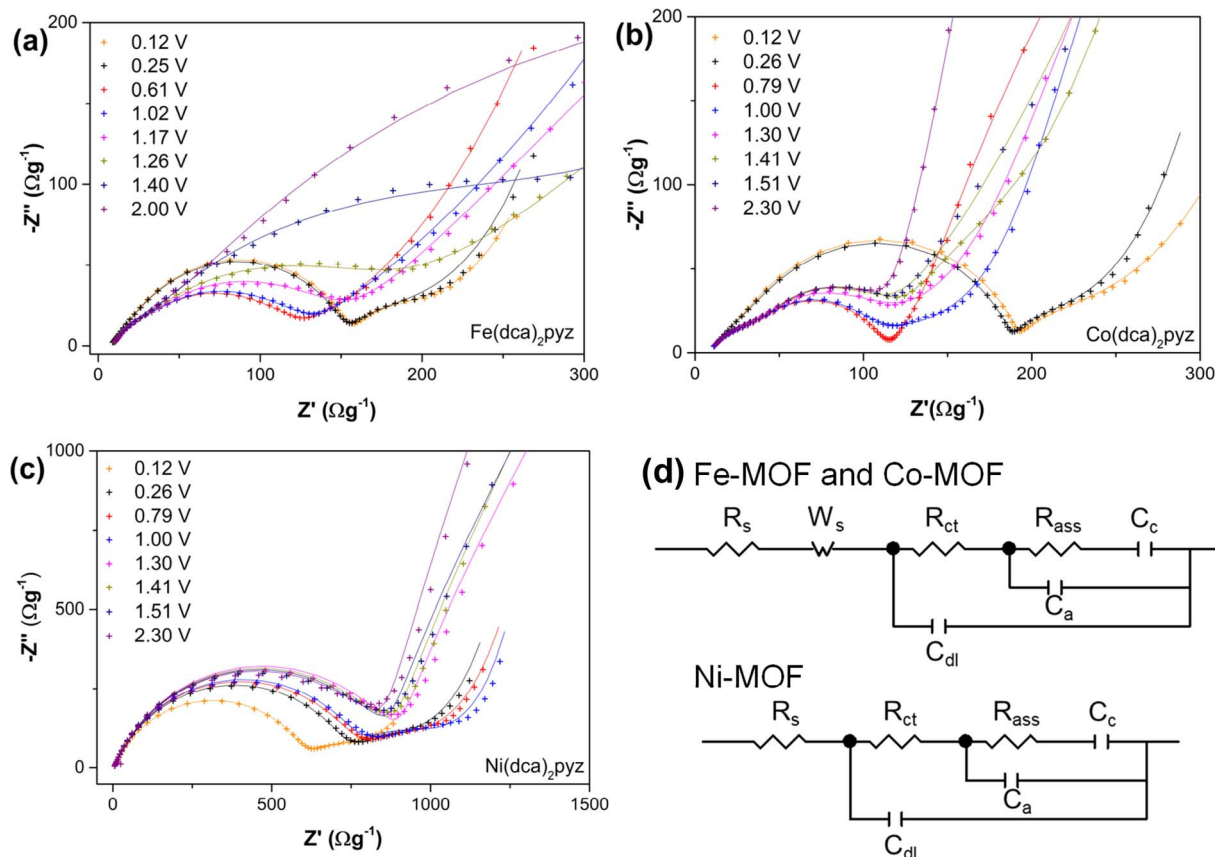


Fig. 7 Nyquist plots of (a)  $\text{Fe}(\text{dca})_2\text{pyz}$ , (b)  $\text{Co}(\text{dca})_2\text{pyz}$  and (c)  $\text{Ni}(\text{dca})_2\text{pyz}$  at the indicated voltages vs.  $\text{Li}/\text{Li}^+$  during the fourth cathodic sweep. The points are the experimental data and the lines the theoretical impedance calculated with the two equivalent circuits represented in (d). The values estimated are depicted in Fig. S13.†





These results show important differences in the mechanism not only in the TM but also in the ligands. Dicyanamide shows strong reduction in Fe-MOF, with the observation of its anion, reduction in Co-MOF but the anionic form is not detected and no detectable reduction in Ni-MOF but decrease of symmetry. In this MOF, the main mechanism for  $\text{Li}^+$  storage seems the interaction with double bonds with the rupture of zwitterion or resonant structure of the ligands, probably in the pyrazine. This mechanism seems to start being relevant in Co-MOF and Fe-MOF at voltages of or below 1 V. Despite the electrochemical activity of the two ligands, individually, the coordination through TMs is clue for obtain high capacity, as charge-discharge plots of the two ligands confirms (Fig. S12†).

Taking all into mind, experimental data indicate that  $\text{Li}^+$  interacts primarily with the ligands in the Ni-MOF, while the Ni is partially oxidized, hindering  $\text{Li}^+$  intercalation. Fe-MOF undergoes partial conversion reaction and shows a high accumulation of negative charges in dca ligand, suggesting that  $\text{Li}^+$  ions likely interact with N atoms in addition to  $\pi$  interactions. Co-MOF displays an intermediate behavior, with Co being reduced but not to the zero oxidation state, and the dca ligand acquiring a negative charge but not in an anionic form. At this point, the question arises whether Co-MOF could behave like Fe-MOF and whether the limitation is kinetic, due to its lower electrical conductivity, or thermodynamic. To answer this question, EIS spectra were measured at different voltages and are illustrated in Fig. 7. Ni-MOF spectra can be fitted to an electric equivalent circuit, characteristic of  $\text{Li}^+$  intercalation within a host material.<sup>59</sup> Following the initial arch linked to charge transfer resistance ( $R_{\text{ct}}$ ) and electrical double-layer capacitance ( $C_{\text{dl}}$ ), the Nyquist plot displays an increase in the imaginary part associated with chemical capacitance ( $C_{\mu}$ ) and its corresponding resistance ( $R_{\text{ass}}$ ). The calculated values are represented in Fig. S13.† Below 1.3 V, the resistance decreases, indicating a flatter impedance, while  $R_{\text{ct}}$  remains in the range of 600–900  $\Omega \text{ g}^{-1}$ , representing the limiting process. Fe-MOF and Co-MOF exhibit distinct spectra, and for a better fitting of the experimental data a Warburg diffusion line is included in the equivalent circuit model for the high-frequency region, followed by the arch assigned to  $C_{\text{dl}}$  and  $R_{\text{ct}}$ . This new element, characteristic of the MOF, is attributed to the resistances of the in-pore electrolyte.<sup>60</sup> The lower  $R_{\text{ct}}$  values observed for Co-MOF ( $\sim 50 \Omega \text{ g}^{-1}$ ) and Fe-MOF ( $\sim 90 \Omega \text{ g}^{-1}$ ) likely explain the observable diffusion, absent in Ni-MOF. In both Co-MOF and Fe-MOF,  $R_{\text{ct}}$  increases below 0.7 V, slightly in Fe-MOF but doubling in Co-MOF. The lower electronic conductivity of Co-MOF and higher electrostatic repulsions explains the higher increase of  $R_{\text{ct}}$  in this MOF. However, the differences are not so high to explain the double storage of  $\text{Li}^+$  in the Fe-MOF respect to the Co-MOF. The fitted chemical capacitance is higher in Fe-MOF than in Co-MOF, suggesting that differences in specific energy density are not solely due to kinetic constraints but also to thermodynamic factors.

## 4 Conclusions

This research highlights the potential of Amorphous Organometallic (AMO) compounds as battery electrodes, which could represent a breakthrough in energy storage technology. These

compounds can be obtained during battery operation by *in situ* amorphization of certain MOFs, without the need of heating the precursors at high temperatures nor using any aggressive chemical reagents. Therefore, AMO compounds can be classified as cost-effective and eco-friendly materials for electrodes.

One of the reasons that just some MOFs can be converted to AMO compounds is assigned to the TM-ligand bond strength. For instance, in this study,  $\text{Fe}(\text{dca})_2\text{pyz}$ ,  $\text{Co}(\text{dca})_2\text{pyz}$ , and  $\text{Ni}(\text{dca})_2\text{pyz}$  MOFs were studied as LIB anodes. The first two became amorphous after lithiation and present a high specific energy density. Looking at the properties, Fe-MOF is the only one of these MOFs with interstitial  $\text{H}_2\text{O}$  molecules (detected by FTIR spectra and TGA measurements) and it also shows large crystals embedded in amorphous phase, as revealed by Raman spectra. These characteristics plausibly explain why Fe-MOF converts into an AMO compound more easily than the other two studied MOFs. In the opposite case, Ni-MOF does not change to an AMO material probably because of the strong Ni–N interaction (as observed by TGA and Raman measurements) and consequently, it presents the lowest specific capacity. Meanwhile, Co-MOF exhibits an intermediate behavior.

In this study, the competitiveness of the iron nitride analog  $\text{Fe}(\text{dca})_2\text{pyz}$  as a cost-effective and environmentally friendly lithium battery anode material is presented. Also, it is demonstrated that some MOFs are capable of transitioning into an amorphous state through lithium incorporation giving rise to novel AMO electrodes, which is beneficial for the electrochemical performance of the electrode. Finally, one of the key parameters for predicting which MOFs can be converted into AMO compounds is given, which is the TM-ligand bond strength. Therefore, this study reveals a promising path for exploring MOFs as electrodes for lithium-ion batteries (LIBs).

## Abbreviations

AMO	AMorphous organometallic
dca	Dicyanamide
pyz	Pyrazine
TMs	Transition metals
TMNs	Transition metal nitrides

## Data availability

The data described in this article and the ESI† will be openly available at Zagan at <https://zagan.unizar.es/collection/articulos?ln=es>, once the manuscript is accepted and published in open access.

## Conflicts of interest

There are no conflicts to declare.

## Acknowledgements

E. J. J.-P. and M. H. acknowledge the funding support from MCIN/AEI/10.13039/501100011033 for the project grant





PID2022-140516OB-I00, E. J. J.-P. for the project grant PID2019-107893RB-I00, and M. H. for CNS2023-145197, PID2019-108247RA-I00, and her Ramón y Cajal fellowship (RYC-2018-025222-I). M. H, I. C.-R and E. J. J.-P acknowledge the Diputación General de Aragón for projects E31\_23R (M. H and I. C.-R.) and T57\_23R (E. J. J.-P.). A. M. acknowledges the Spanish ministry of Science and Universities (RYC2018-024561-I, CNS2023-144346), and the Gobierno de Aragón (Nanomidas group, E13\_23R). The authors would like to acknowledge the use of Servicio General de Apoyo a la Investigación-SAI, as well as the use of instrumentation and technical advice provided by the National Facility ELCMI ICTS node "Laboratorio de Microscopias Avanzadas" of the Universidad de Zaragoza.

## References

- 1 S. Natarajan, R. M. Bhattarai, M. S. P. Sudhakaran, Y. S. Mok and S. J. Kim, *J. Power Sources*, 2023, **577**, 233170.
- 2 E. A. Olivetti, G. Ceder, G. G. Gaustad and X. Fu, *Joule*, 2017, **1**, 229–243.
- 3 T. Vook, S. C. Dey, J. Yang, M. Nimlos, S. Park, S. D. Han and W. J. Sagues, *J. Energy Storage*, 2023, **73**, 109242.
- 4 Y. Liu, H. Shi and Z. S. Wu, *Energy Environ. Sci.*, 2023, **16**, 4834–4871.
- 5 Y. Dong, B. Wang, K. Zhao, Y. Yu, X. Wang, L. Mai and S. Jin, *Nano Lett.*, 2017, **17**, 5740–5746.
- 6 Y. Dong, Y. Li, H. Shi, J. Qin, S. Zheng, R. He and Z. S. Wu, *Carbon*, 2020, **159**, 213–220.
- 7 P. Yu, L. Wang, F. Sun, D. Zhao, C. Tian, L. Zhao, X. Liu, J. Wang and H. Fu, *Chem.–Eur. J.*, 2015, **21**, 3249–3256.
- 8 B. K. Kang, Y. J. Choi, H. W. Choi, S. Bin Kwon, S. Kim, Y. J. Kim, J. S. Park, W. S. Yang, D. H. Yoon and W. H. Ryu, *Chem. Eng. J.*, 2021, **420**, 129630.
- 9 M. Idrees, A. S. Haidyrah, Ata-ur-Rehman, Q. Zhang, X. Li and S. M. Abbas, *J. Alloys Compd.*, 2021, **883**, 160824.
- 10 H. Huang, S. Gao, A. M. Wu, K. Cheng, X. N. Li, X. X. Gao, J. J. Zhao, X. L. Dong and G. Z. Cao, *Nano Energy*, 2017, **31**, 74–83.
- 11 L. Lai, J. Zhu, B. Li, Y. Zhen, Z. Shen, Q. Yan and J. Lin, *Electrochim. Acta*, 2014, **134**, 28–34.
- 12 P. Wang, J. Bai, K. Li, H. Ma, W. Li, X. Zhu, Y. Sun and B. Zhao, *Chem. Eng. J.*, 2021, **425**, 130607.
- 13 X. Li, C. Deng, H. Wang, J. Si, S. Zhang and B. Huang, *ACS Appl. Mater. Interfaces*, 2021, **13**, 7297–7307.
- 14 B. Das, M. V. Reddy, G. V. S. Rao and B. V. R. Chowdari, *J. Mater. Chem.*, 2012, **22**, 17505–17510.
- 15 R. Zou, M. Xu, S. A. He, X. Han, R. Lin, Z. Cui, G. He, D. J. L. Brett, Z. X. Guo, J. Hu and I. P. Parkin, *J. Mater. Chem. A*, 2018, **6**, 19853–19862.
- 16 T. Wang, G. Chen, X. Liu, F. Chen, N. Zhang, J. Li, S. Liang, R. Ma and G. Qiu, *ACS Appl. Energy Mater.*, 2018, **1**, 4432–4439.
- 17 L. Tian, Y. Xie, J. Lu, T. Liu, Q. Hu, Y. Xiao, X. Zhu and X. Su, *J. Alloys Compd.*, 2022, **922**, 166208.
- 18 G. Jiang, H. Han, W. Zhuang, X. Xu, S. Kaskel, F. Xu and H. Wang, *J. Mater. Chem. A*, 2019, **7**, 17561–17569.
- 19 Y. G. Weng, Z. H. Ren, Z. R. Zhang, J. Shao, Q. Y. Zhu and J. Dai, *Inorg. Chem.*, 2021, **60**, 17074–17082.
- 20 Y. Jin, C. Zhao, Z. Sun, Y. Lin, L. Chen, D. Wang and C. Shen, *RSC Adv.*, 2016, **6**, 30763–30768.
- 21 K. Wang, J. Chen, F. Hou, H. Wang, Y. Zhang, X. Zhong, Y. Song, Y. Zhang, Z. Zhang, H. Liu, J. Liang and H. Wang, *Chem. Eng. J.*, 2023, **455**, 140561.
- 22 H. Yue, Z. Shi, Q. Wang, Z. Cao, H. Dong, Y. Qiao, Y. Yin and S. Yang, *ACS Appl. Mater. Interfaces*, 2014, **6**, 17067–17074.
- 23 C. Li, L. Liu, J. Kang, Y. Xiao, Y. Feng, F. F. Cao and H. Zhang, *Energy Storage Mater.*, 2020, **31**, 115–134.
- 24 X. Tang, C. Liu, H. Wang, L. P. Lv, W. Sun and Y. Wang, *Coord. Chem. Rev.*, 2023, **494**, 215361.
- 25 R. Shah, S. Ali, F. Raziq, S. Ali, P. M. Ismail, S. Shah, R. Iqbal, X. Wu, W. He, X. Zu, A. Zada, Adnan, F. Mabood, A. Vinu, S. H. Jhung, J. Yi and L. Qiao, *Coord. Chem. Rev.*, 2023, **477**, 214968.
- 26 R. Zhao, Z. Liang, R. Zou and Q. Xu, *Joule*, 2018, **2**, 2235–2259.
- 27 R. C. K. Reddy, J. Lin, Y. Chen, C. Zeng, X. Lin, Y. Cai and C. Y. Su, *Coord. Chem. Rev.*, 2020, **420**, 213434.
- 28 A. García-Fernández, J. M. Bermúdez-García, S. Castro-García, R. Artiaga, J. López-Beceiro, M. A. Señaris-Rodríguez and M. Sánchez-Andújar, *Polyhedron*, 2016, **114**, 249–255.
- 29 P. Jensen, S. R. Batten, B. Moubaraki and K. S. Murray, *J. Solid State Chem.*, 2001, **159**, 352–361.
- 30 P. He, L. Hao, N. Liu, H. Bai, R. Niu and J. Gong, *Chem. Eng. J.*, 2021, **423**, 130268.
- 31 P. He, H. Bai, Z. Fan, L. Hao, N. Liu, B. Chen, R. Niu and J. Gong, *J. Mater. Chem. A*, 2022, **10**, 13378–13392.
- 32 Y. Zhang, P. Wang, J. Yang, K. Li, N. Zhang, G. Liu, Y. Duan and J. Qiu, *J. Colloid Interface Sci.*, 2022, **613**, 733–746.
- 33 L. Ma, R. Wang, Y. H. Li, X. F. Liu, Q. Q. Zhang, X. Y. Dong and S. Q. Zang, *J. Mater. Chem. A*, 2018, **6**, 24071–24077.
- 34 Y. Qiu, H. Yang, B. Wen, L. Ma and Y. Lin, *J. Colloid Interface Sci.*, 2021, **590**, 561–570.
- 35 V. Prakash, K. Srivastava and J. Prasad, *Indian J. Chem., Sect. A: Inorg., Bio-inorg., Phys., Theor. Anal. Chem.*, 2017, **56A**, 585–591.
- 36 J. W. Jurss, R. S. Khnayzer, J. A. Panetier, K. A. El Roz, E. M. Nichols, M. Head-Gordon, J. R. Long, F. N. Castellano and C. J. Chang, *Chem. Sci.*, 2015, **6**, 4954–4972.
- 37 P. Nie, L. Shen, H. Luo, B. Ding, G. Xu, J. Wang and X. Zhang, *J. Mater. Chem. A*, 2014, **2**, 5852–5857.
- 38 D. Sun, H. Wang, B. Deng, H. Zhang, L. Wang, Q. Wan, X. Yan and M. Qu, *Carbon*, 2019, **143**, 706–713.
- 39 M. J. Piernas-Muñoz, E. Castillo-Martínez, V. Roddatis, M. Armand and T. Rojo, *J. Power Sources*, 2014, **271**, 489–496.
- 40 P. Xiong, G. Zeng, L. Zeng and M. Wei, *Dalton Trans.*, 2015, **44**, 16746–16751.
- 41 Y. Tang, J. Hu, H. Tao, Y. Li, W. Li, H. Li, M. Zhou, K. Wang and K. Jiang, *J. Alloys Compd.*, 2022, **891**, 161867.
- 42 L. Shen, Z. Wang and L. Chen, *Chem.–Eur. J.*, 2014, **20**, 12559–12562.



- 43 F. A. Mautner, J. H. Albering, M. Mikuriya and S. S. Massoud, *Inorg. Chem. Commun.*, 2010, **13**, 796–799.
- 44 J. Sánchez-González, A. Macías-García, M. F. Alexandre-Franco and V. Gómez-Serrano, *Carbon*, 2005, **43**, 741–747.
- 45 J. Hu, H. Tao, M. Chen, Z. Zhang, S. Cao, Y. Shen, K. Jiang and M. Zhou, *ACS Appl. Mater. Interfaces*, 2022, **14**, 12234–12242.
- 46 P. Jensen, S. R. Batten, B. Moubaraki and K. S. Murray, *J. Chem. Soc., Dalton Trans.*, 2002, 3712–3722.
- 47 M. Maczka, A. Gagor, M. Ptak, D. Stefańska and A. Sieradzki, *Phys. Chem. Chem. Phys.*, 2018, **20**, 29951–29958.
- 48 D. W. Keefer, H. Gou, A. P. Purdy, A. Epshteyn, D. Y. Kim, J. V. Badding and T. A. Strobel, *J. Phys. Chem. A*, 2016, **120**, 9370–9377.
- 49 L. Sun, M. G. Campbell and M. Dince, *Angew. Chem., Int. Ed.*, 2016, **55**, 3566–3579.
- 50 F. Wu, J. Maier and Y. Yu, *Chem. Soc. Rev.*, 2020, **49**, 1569–1614.
- 51 H. Li, P. Balaya and J. Maier, *J. Electrochem. Soc.*, 2004, **151**, A1878.
- 52 F. Martinez-Julian, A. Guerrero, M. Haro, J. Bisquert, D. Bresser, E. Paillard, S. Passerini and G. Garcia-Belmonte, *J. Phys. Chem. C*, 2014, **118**, 6069–6076.
- 53 I. Ciria-Ramos, I. Tejedor, L. Caparros, B. Doñagueda, O. Lacruz, A. Urtizberea, O. Roubeau, I. Gascón and M. Haro, *Dalton Trans.*, 2023, **52**, 7196–7207.
- 54 X. Liu and J. Liu, *Corros. Sci.*, 2017, **115**, 129–134.
- 55 X. Zhang, L. Guo, L. Gan, Y. Zhang, J. Wang, L. R. Johnson, P. G. Bruce and Z. Peng, *J. Phys. Chem. Lett.*, 2017, **8**, 2334–2338.
- 56 Y. Tang, W. Li, P. Feng, M. Zhou, K. Wang and K. Jiang, *Chem. Eng. J.*, 2020, **396**, 125269.
- 57 S. Wheeler, I. Capone, S. Day, C. Tang and M. Pasta, *Chem. Mater.*, 2019, **31**, 2619–2626.
- 58 S. P. Kelley and R. D. Rogers, *Inorg. Chem.*, 2015, **54**, 10323–10334.
- 59 N. Vicente, M. Haro and G. Garcia-Belmonte, *Chem. Commun.*, 2018, **54**, 1025–1040.
- 60 S. Bi, H. Banda, M. Chen, L. Niu, M. Chen, T. Wu, J. Wang, R. Wang, J. Feng, T. Chen, M. Dincă, A. A. Kornyshev and G. Feng, *Nat. Mater.*, 2020, **19**, 552–558.

